ACS APPLIED MATERIALS & INTERFACES

Research Article

www.acsami.org

Template and Silica Interlayer Tailorable Synthesis of Spindle-like Multilayer α-Fe_2O_3/Ag/SnO_2 Ternary Hybrid Architectures and Their Enhanced Photocatalytic Activity

Lingling Sun,[†] Wei Wu,*[,‡] Shuanglei Yang,[§] Juan Zhou,[†] Mengqing Hong,[†] Xiangheng Xiao,[†] Feng Ren,[†] and Changzhong Jiang*[,†]

[†]Key Laboratory of Artificial Micro- and Nano-structures of Ministry of Education, School of Physics and Technology, Wuhan University, Wuhan, Hubei 430072, P. R. China

[‡]Laboratory of Functional Nanomaterials and Printing Electronics, School of Printing and Packaging, Wuhan University, Wuhan, Hubei 430072, P. R. China

[§]State Key Laboratory for Powder Metallurgy, Central South University, Changsha, Hunan 410083, P. R. China

Supporting Information

ABSTRACT: Our study reports a novel iron oxide/noble metal/semiconductor ternary multilayer hybrid structure that was synthesized through template synthesis and layer-by-layer deposition. Three different morphologies of α-Fe_2O_3/Ag/SiO_2/SnO_2 hybrid architectures were obtained with different thicknesses of the SiO_2 interlayer which was introduced for tailoring and controlling the coupling of noble metal Ag nanoparticles (NPs) with the SnO_2 semiconductor. The resulting samples were characterized in terms of morphology, composition, and optical property by various analytical techniques. The as-obtained α-Fe_2O_3/Ag/SiO_2/SnO_2 nanocomposites exhibit enhanced visible light or UV photocatalytic abilities, remarkably superior to commercial pure SnO_2 products, bare α-Fe_2O_3 seeds, and α-Fe_2O_3/SnO_2 nanocomposites. Moreover, the sample of α-Fe_2O_3/Ag/SiO_2/SnO_2 also exhibits good chemical stability and recyclability because it has higher photocatalytic activity even after eight cycles. The origin of enhanced photocatalytic activity on the multilayer core−shell α-Fe_2O_3/Ag/SiO_2/SnO_2 nanocomposites was primarily ascribed to the coupling between noble metal Ag and the two semiconductors Fe_2O_3 and SnO_2, which are proven to be applied in recyclable photocatalysis.

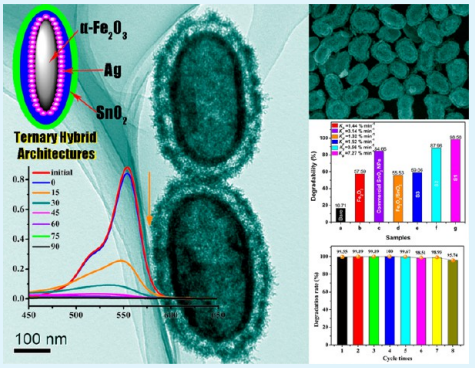

KEYWORDS: *iron oxide, noble metal, SiO_2 interlayer, heterostructures, photocatalytic activity*

INTRODUCTION

Semiconductor photocatalysis has attracted growing research efforts due to its important application in counteracting the worldwide energy shortage and environmental pollution. Owing to its low cost, relatively high catalytic activity, low toxicity, and high chemical stability, many semiconductor oxides such as TiO_2, SnO_2, Fe_2O_3, WO_3, ZnO, and ZrO_2 were widely used in photocatalytic degradation,[1−8] but the single-component semiconductor has a number of disadvantageous features including low light harvesting, high recombination rate of electron−hole pairs, and hardly being able to be separated and recycled. For example, pure TiO_2 and SnO_2 are wide-band gap semiconductors and absorb only UV light to generate electron−hole pairs, which greatly limit their photocatalytic activity.

Therefore, in recent years, more attention and research have been paid to combine a variety of different semiconductor components and ion doping or introduce noble metals in order to precisely control nanostructures and the corresponding properties. Among the above methods, hybrid semiconductor composites especially the p−n-type heterostructures and combining two semiconductors with narrow and wide bandgap heterostructures show improved photocatalytic abilities over their single-component counterparts. It not only enhances light harvesting but also reduces the recombination of photogenerated charges by changing the photocatalytic materials from a single type of semiconductor oxide to composites. For example, various semiconductor nanocomposites including ZnO/SnO_2,[9−11] TiO_2/Fe_2O_3,[12−14] SnO_2/Fe_2O_3,[15] and TiO_2/SnO_2[16] have been reported and exhibited enhanced photocatalytic abilities.[17,18] Hematite (α-Fe_2O_3), one of the commonly used and chemically stable magnetic iron oxide materials, is an n-type semiconductor with a band gap of 2.2 eV and can absorb part of visible light. Recent studies have revealed that the physical performances of SnO_2 or Fe_2O_3 can be remarkably improved by forming Fe_2O_3−SnO_2 hetero-

Received: October 24, 2013
Accepted: December 26, 2013
Published: December 26, 2013

structures.[19] Especially in photocatalytic application, it is well established that the α-Fe_2O_3/SnO_2 hybrid heterostructures not only extend the range of light absorption from the UV region to the visible region but also effectively mitigate the recombination between photogenerated electron−hole pairs.[20] That is because the photogenerated electrons in the conduction band of α-Fe_2O_3 tend to transfer to SnO_2, which can promote the separation of photogenerated electrons and holes. In addition, the α-Fe_2O_3/SnO_2 hybrid heterostructures will be confirmed in the magnetic recycling photocatalysts application because α-Fe_2O_3 can be easily converted to magnetite (Fe_3O_4) and therefore be separated from the reaction. For example, Niu and co-workers have synthesized branched SnO_2/α-Fe_2O_3 semiconductor nanoheterostructures (SNHs) by a hydrothermal strategy, and the SnO_2/α-Fe_2O_3 SNHs exhibited excellent visible light or UV photocatalytic abilities superior to their α-Fe_2O_3 precursor due to the effective electron−hole separation at the SnO_2/α-Fe_2O_3 interfaces.[21] In our previous work, the hollow iron oxide/SnO_2 and γ-Fe_2O_3@SnO_2 nanoparticles (NPs) also exhibit the clear enhanced photocatalytic activity, and the composite NPs can be fastly separated and have good recyclability.[22,23]

Because noble metal doping in the single semiconductor can extend the region of optical response, introduce the localized surface plasmon resonance (LSPR) effect, and finally enhance the photocatalytic activity, the noble metal/semiconductor photocatalytic system has gained increasing interest and attention. A noble metal has a high catalytic activity because of its structure, absorbable surface, and the as-formed "active compound" intermediate between that of molecules and of bulk material.[24] In addition, the noble metal nanomaterials have a strong local electric field on the surface and can enhance the interaction between light and the surface of NPs. Therefore, the introduction of noble metal (such as Au, Ag, Pt) can also change electron distribution in the above system and affect the surface properties of the semiconductor material, thereby improving the photocatalytic activity.[25−27] In the noble metal-semiconductor photocatalytic system, the photoexcited plasmonic energy in the metal is transferred to the semiconductor, generating electron−hole pairs in the semiconductor. Charge separation can occur either via the transfer of hot electrons known as direct electron transfer (DET) or via the plasmon-induced resonant energy transfer (PIRET).[28,29] For instance, if Ag NPs doped with the semiconductor NPs are used for the photocatalyst, visible light absorption by silver plasmon is thought to induce electron transfer to the semiconductor resulting in separation of electron−hole pairs and thus activation by visible light. Therefore, the final photocatalytic activity can be improved by introducing noble metal NPs in a single semiconductor material. For example, the as-synthesized Ag@TiO_2 core−shell nanocomposite has a higher photocatalytic activity under visible light irradiation compared to the pure TiO_2.[30] Moonsiri and co-workers have compared the effect of Pt and Ag on the photocatalytic degradation, and the results revealed that the photocatalytic performance of TiO_2−Ag was better than that of TiO_2−Pt owing to the ability of Ag to produce more superoxide radicals and to the increased rate of direct hole oxidation.[31]

However, to the best of our knowledge, the synthesis of the magnetic iron oxide-noble metal-semiconductor ternary photocatalytic system remains scarce in the literature. Herein, a new type of hybrid architecture, α-Fe_2O_3/Ag/SiO_2/SnO_2 ternary core−shell nanocomposite has been prepared. In the multilayer core−shell structure, the coupling effect of the interface between noble metal and semiconductor has been tailored by a silica interlayer with different thicknesses, and the related photocatalytic properties have been investigated. The photocatalytic results illustrate that the as-obtained α-Fe_2O_3/Ag/SiO_2/SnO_2 nanocomposites exhibit enhanced photocatalytic activities compared with the commercial SnO_2 nanopowders, the pure α-Fe_2O_3 seeds, and α-Fe_2O_3/SnO_2 nanocomposites. In particular, the samples with the thickest SiO_2 interlayer represent the highest photocatalytic activity under illumination of UV and visible mixed light, which presents good chemical stability and recyclability even after eight cycles. Additionally, the α-Fe_2O_3/Ag/SnO_2 exhibits a better visible light driven photocatalytic ability. There is a striking difference between the samples with and without SiO_2 interlayers, and the results illustrate the silica interlayers can be used to control and adjust the photocatalytic activity under different light sources. The corresponding photocatalytic mechanisms are proposed and discussed.

EXPERIMENTAL SECTION

Materials. Ferric chloride hexahydrate ($FeCl_3·6H_2O$), sodium dihydrogen phosphate ($NaH_2PO_4·2H_2O$), disodium hydrogen phosphate ($Na_2HPO_4·12H_2O$), glutaraldehyde aqueous solution ($C_5H_8O_2$, 25%), silver nitrate ($AgNO_3$), urea ($CO(NH_2)_2$), ethylene glycol (EG) and ethanol (C_2H_5OH) were purchased from Sinopharm Chemical Reagent Co., Ltd. Ammonia ($NH_3·H_2O$, 25%) was purchased from Wuhan Wangsen Chemical Reagent Co., Ltd. 3-Aminopropyltrimethoxysilane (ATPES), ethyl silicate (TEOS), potassium stannate trihydrate ($K_2SnO_3·3H_2O$), and Rhodamine B (RhB) were purchased from Shanghai Jingchun Chemical Reagent Co., Ltd. All the used reagents were analytically pure (AR) without further purification. The deionized water was used throughout the experiments.

Synthesis of Spindle-Like α-Fe_2O_3 Seeds. Spindle-like α-Fe_2O_3 NPs were synthesized following our previous method.[32] Briefly, the aqueous NaH_2PO_4 solution (100 mL, 0.45 mM) was heated to 95 °C, and then, 1.8 mL of $FeCl_3$ (1.48 M) was added dropwise into the solution. The mixture solution was kept at 105 °C for 14 h. The product was centrifuged and washed several times with ethanol and deionized water and then dried at 70 °C for further use.

Synthesis of α-Fe_2O_3/Ag Composite NPs. The α-Fe_2O_3/Ag composite NPs were synthesized by a step-by-step method.[33] The first step is fabrication of amino functionalized α-Fe_2O_3 NPs: namely, 10 mg of α-Fe_2O_3 seeds was dispersed in 100 mL of ethanol, and then, 0.5 mL of ATPES aqueous solution (2%, v/v) and 1 mL of water were added under stirring at 30 °C for 2 h; the obtained resultants were centrifuged and washed twice with ethanol. Then, aldehyde functionalized α-Fe_2O_3 NPs were fabricated: the as-obtained amino functionalized α-Fe_2O_3 NPs were dispersed in the mixture (5 mL of glutaraldehyde aqueous solution (25%) and 2 mL of phosphate buffer (PB) solution (0.02 M)) with rapid stirring at 30 °C for 2 h; the resultants were centrifuged and washed twice with ethanol and water. For depositing Ag NPs on the α-Fe_2O_3 nanospindles, the obtained aldehyde-terminated Fe_2O_3 was dispersed in 3 mL of ethanol; then, 34 mg of silver nitrate was dissolved into 5 mL of deionized water in test tubes, and diluted ammonia (4%) was gradually added into the $AgNO_3$ solution until the generated precipitates completely vanished. Then, the aldehyde-terminated Fe_2O_3 ethanol solution and the above as-prepared solution were mixed and heated at 80 °C for 40 min; when the reaction ended, the obtained solution was centrifuged and washed twice with ethanol and water and then dried at 70 °C for subsequent treatments.

Synthesis of α-Fe_2O_3/Ag/SiO_2 Composite NPs. A modified Stöber method has been used to synthesize the silica coated α-Fe_2O_3/Ag composite NPs. Briefly, 20 mg of α-Fe_2O_3/Ag NPs was first dispersed in a mixed solution (consisting of 40 mL of ethanol and 10 mL of deionized water) by ultrasonication, and then, 1 mL of ammonia was

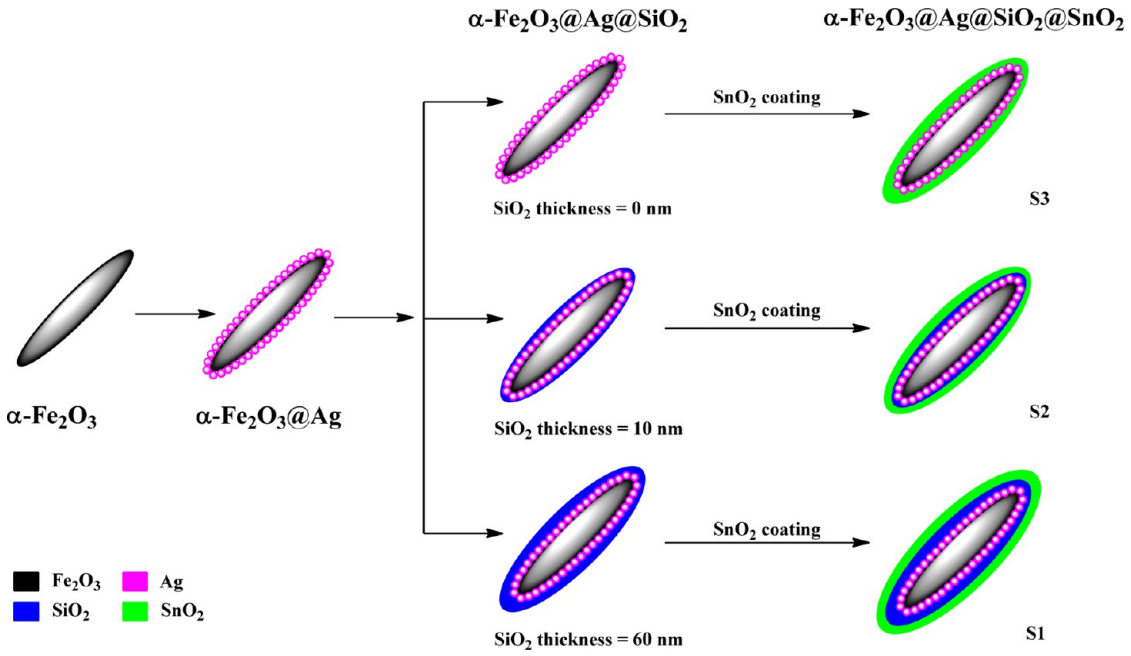

Figure 1. Schematic procedure for the fabrication of core–shell α-Fe_2O_3/Ag/SiO_2/SnO_2 nanocomposites.

added to the mixed solution. Under magnetic stirring, 0.6 mL of TEOS was added to the above mixed solution and the reaction was continued for 4 h at 25 °C. Finally, the α-Fe_2O_3/Ag/SiO_2 NPs were harvested by centrifugation and washed with ethanol and water several times. The as-synthesized product was characterized by TEM and SEM, and the results show that the thickness of SiO_2 shell deposited on the α-Fe_2O_3/Ag NPs was approximately 60 nm; thus, it was named as the α-Fe_2O_3/Ag/SiO_2 (ST = 60 nm) NP. By only decreasing the volume of TEOS to 0.1 mL, the corresponding product was observed to have a thinner SiO_2 shell (SiO_2 thickness, ca. 10 nm) and thus named as the α-Fe_2O_3/Ag/SiO_2 (ST = 10 nm) NP.

Synthesis of α-Fe_2O_3/Ag/SiO_2/SnO_2 Nanocomposites. Twenty mg of α-Fe_2O_3/Ag/SiO_2 (ST = 60 nm or ST = 10 nm) NPs was dispersed in 25 mL of ethanol/water (37.5 v/v % ethanol) mixed solvent. Then, 0.375 g of urea and 75 mg of $K_2SnO_3{\cdot}3H_2O$ were added. After stirring for about 10 min under room temperature until all salts dissolved, the suspension was transferred to a 50 mL Teflon-lined stainless-steel autoclave, which was then heated in an air flow electric oven at 170 °C for 24 h. Finally, after the autoclave cooled down naturally, the products were washed with ethanol and water twice. The obtained products encapsulated with α-Fe_2O_3/Ag/SiO_2 (ST = 60 nm) and (ST = 10 nm) were labeled as S1 and S2, respectively. For the obtained α-Fe_2O_3/Ag/SnO_2 nanocomposites, 10 mg of α-Fe_2O_3/Ag (ST = 0) particles, 0.75 g of urea, and 75 mg of $K_2SnO_3{\cdot}3H_2O$ were dispersed in the mixed solution containing 15 mL of ethylene glycol and 8 mL of water and then heated for 12 h at 170 °C in a 30 mL Teflon-lined stainless-steel autoclave. The obtained resultant was washed with ethanol and water twice and labeled as S3. As a comparison, the α-Fe_2O_3/SnO_2 nanocomposites (without silver NPs) were synthesized by the hydrothermal method with the α-Fe_2O_3 seeds as starting template, which is the same to the synthesis process of the samples S1 and S2.

Characterization. Scanning electron microscopy (SEM) images were obtained by using a high resolution field emission SEM (FEI Nova-400). The transmission electron microscopy (TEM) patterns were measured by JEOL JEM-2010 (HT) operated at 200 kV. The high-resolution transmission electron microscopy (HRTEM) and energy-dispersive X-ray spectroscopy (EDX) analysis were performed with a JEOL JEM-2100F. Powder X-ray diffraction (XRD) patterns of the samples were recorded on a D/ruax2550PC (Japan) using Cu Kα radiation (λ = 0.1542 nm) operated at 40 kV and 40 mA and at a scan rate of 0.05° 2θ S^{-1}. X-ray photoelectron spectroscopy (XPS) analysis was performed on a Thermo Scientific ESCALAB 250Xi system with Al Kα (1486.6 eV) as the radiation source. The absorption spectra of the samples were carried out on a Shimadzu UV-2550 spectrophotometer.

Photocatalytic Tests. In the photocatalytic experiments under UV and visible mixed light, 3 mg of the obtained samples were redispersed in 10 mL of the RhB solution (10 mg·L^{-1}) and the mixed solution was stored in the dark for 30 min with gentle stirring to reach the absorption equilibrium. Then, the solutions were illuminated under a mercury lamp (300 W). The reaction solutions were sampled at 15 min illumination intervals, and the corresponding UV–visible spectra (measured in the range of 450 to 650 nm) were recorded to monitor the progress of the degradation of RhB by a Shimadzu 2550 UV–visible spectrophotometer. (A 10 mg·L^{-1} RhB solution without added particles was subjected to the same test, as a control.) The photocatalytic experiment under UV light irradiation or visible light irradiation was the same as the process of UV and visible mixed light via adding the respective UV short pass filter or visible light short pass filter, and the reaction time was prolonged to 180 min. The UV light (λ < 420 nm) or visible light (λ > 420 nm) source came from a mercury lamp (300 W) of BL-GHX-V photochemical reaction apparatus, and the spectral distribution and relative intensity of the mercury lamp were listed in Table S1 (in the Supporting Information).

RESULTS AND DISCUSSION

Figure 1 illustrates the procedure for generating the novel multilayer core–shell nanocomposites. In the process, spindle-like α-Fe_2O_3 NPs are coated with uniform Ag NPs by the self-catalytic growth method. The size and amount of Ag NPs deposited on the surface of α-Fe_2O_3 NPs can be controlled by the reaction time. Then, the α-Fe_2O_3/Ag NPs are capsulated with a layer of SiO_2 by a modified Stöber method. The thickness of the SiO_2 layer can be tailored by changing the additive amount of TEOS. Herein, we obtained three different thicknesses of SiO_2 shell (SiO_2 thickness (ST) = 0, ST = 10 nm, and ST = 60 nm). Silica coating with different thicknesses not only tailors the spacing between noble metal and semiconductor and thus influences the coupling effect but also modifies the surface properties, which is beneficial to subsequent hydrothermal deposition of SnO_2 forming uniform

dx.doi.org/10.1021/am404700h | ACS Appl. Mater. Interfaces 2014, 6, 1113–1124

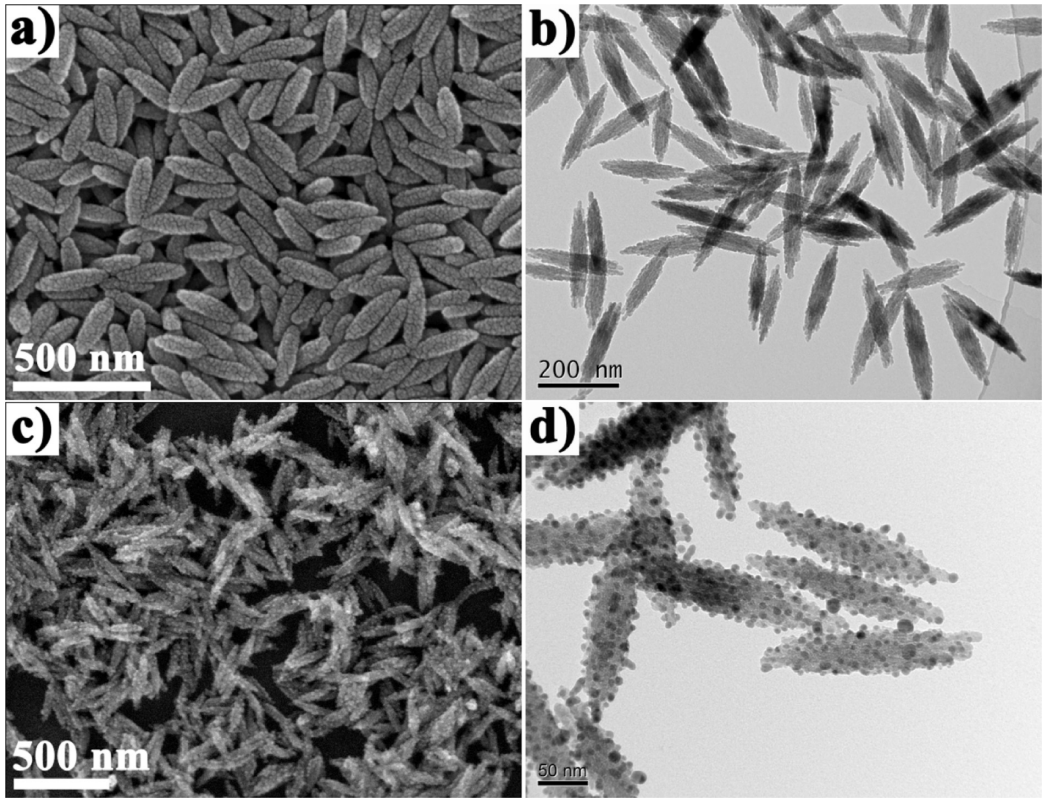

Figure 2. SEM and TEM images of as-synthesized spindle-like hematite seeds (a, b) and Ag-coated hematite composite NPs (c, d), respectively.

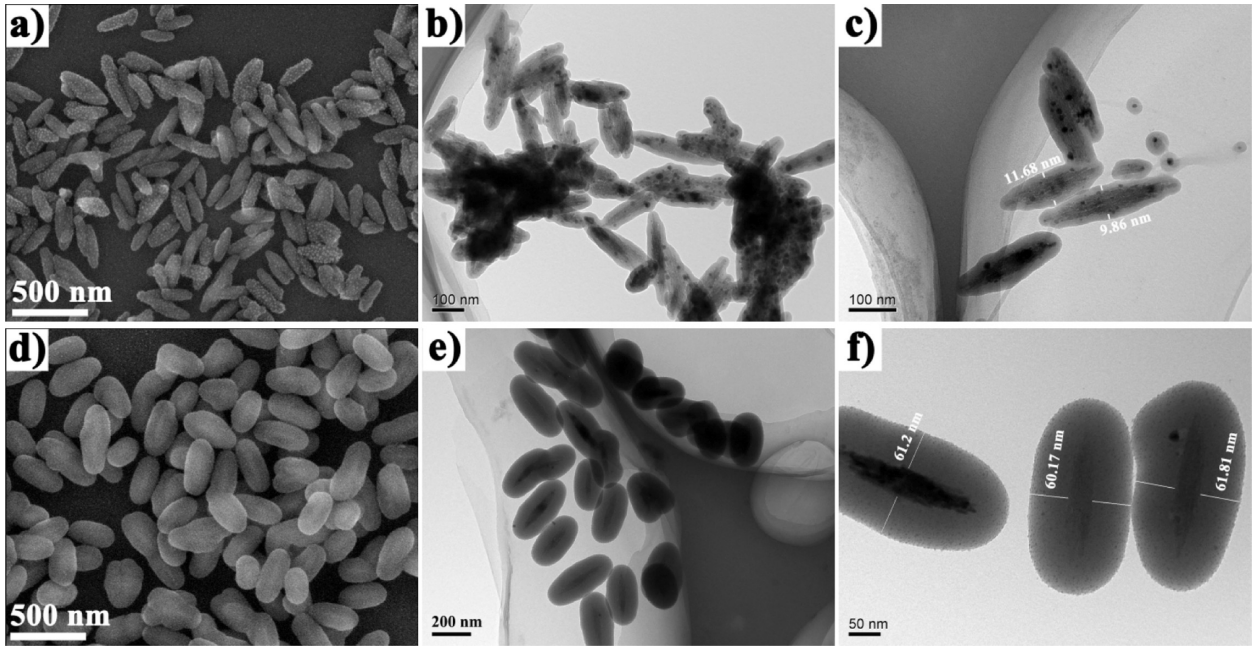

Figure 3. SEM and TEM images of the α-Fe_2O_3/Ag/SiO_2 NPs with the SiO_2 thickness of ca. 10 nm (a–c) and the SiO_2 thickness of ca. 60 nm (d–f).

shells. Finally, multilayer α-Fe_2O_3/Ag/SiO_2/SnO_2 core–shell nanocomposites are fabricated by a hydrothermal method. The α-Fe_2O_3/Ag/SiO_2/SnO_2 nanocomposites with different morphologies and properties are obtained by using the template of α-Fe_2O_3/Ag/SiO_2 NPs with different thicknesses of the silica layer to grow the SnO_2 shell.

Figure 2a,b is the SEM and TEM images of as-synthesized α-Fe_2O_3 seeds, respectively, which clearly show that the monodispersed α-Fe_2O_3 NPs possess a spindle-like shape and uniform size with a length of ca. 240 nm and a width of ca. 50 nm. Figure 2c shows the SEM image of the sample after coating with Ag NPs; it can be seen that many small Ag NPs are evenly deposited on the surface of α-Fe_2O_3 NPs, which can be further

dx.doi.org/10.1021/am404700h | ACS Appl. Mater. Interfaces 2014, 6, 1113–1124

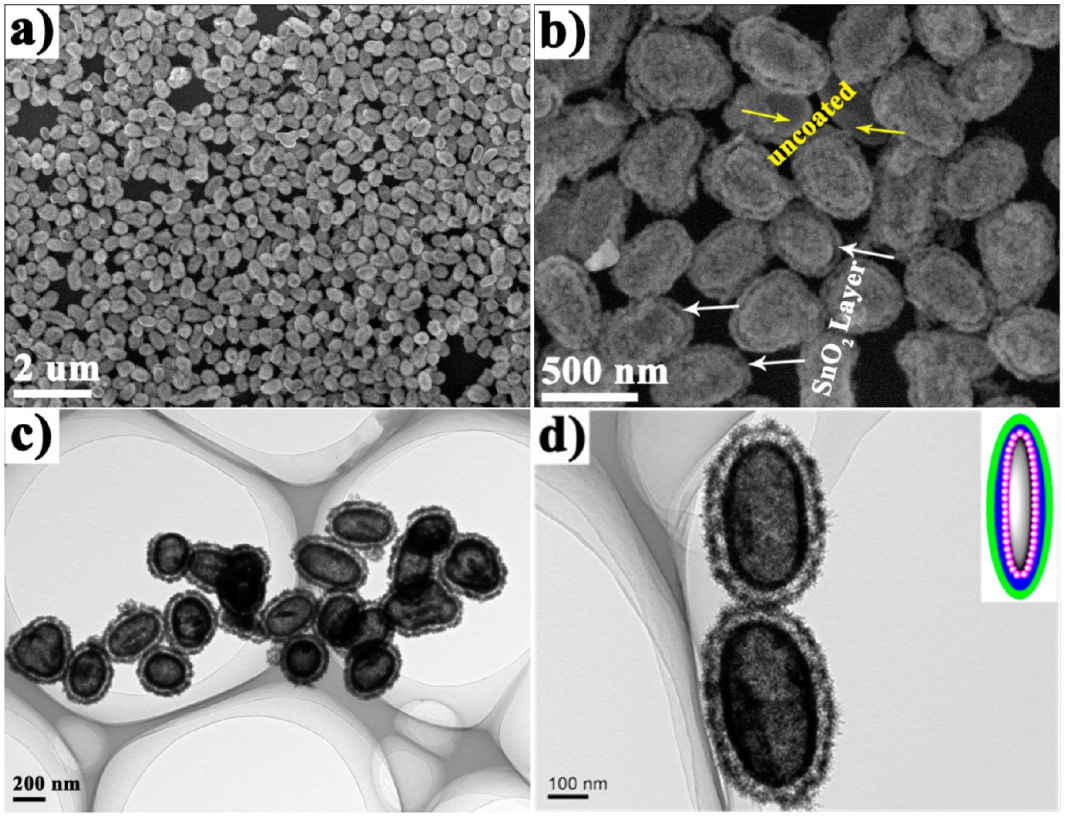

Figure 4. SEM images (a, b) and TEM images (c, d) of α-Fe_2O_3/Ag/SiO_2/SnO_2 (sample S1) nanocomposites.

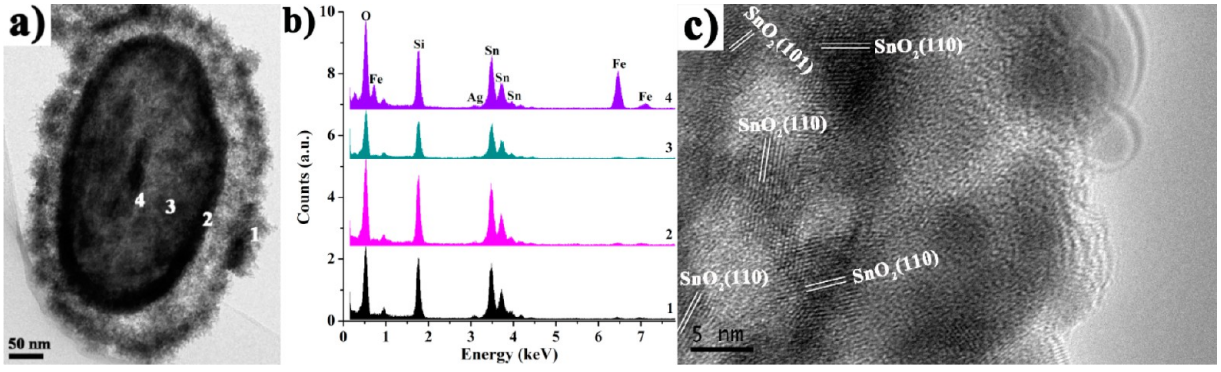

Figure 5. HRTEM image of a single α-Fe_2O_3/Ag/SiO_2/SnO_2 (S1) nanoparticle (a); EDX spectra taken from spots 1, 2, 3, and 4 in (a), respectively (b); HRTEM image showing the lattice fringes taken from the edge of the S1 nanoparticle (c).

proved by the TEM image and corresponding SAED analysis (as shown in Figure 2d). Furthermore, it can be found by close observation that the size of Ag nanocrystals is small and mainly concentrated at 5−10 nm by calculation from the corresponding TEM image, and the average size is ca. 5.9 nm.

Figure 3 shows the SEM and TEM images of the α-Fe_2O_3/Ag samples after coating with the SiO_2. In this step, the thickness of the SiO_2 layer can be controlled by adjusting the added amount of TEOS. As shown in Figure 3a, the α-Fe_2O_3/Ag/SiO_2 NPs are synthesized by added 0.1 mL of TEOS. The Ag NPs are still located on the surface of α-Fe_2O_3, and the morphology of α-Fe_2O_3/Ag/SiO_2 (ST = 10 nm) NPs is similar to the α-Fe_2O_3/Ag NPs due to the thinness of SiO_2 layers. However, the size of α-Fe_2O_3/Ag/SiO_2 (ST = 10 nm) NPs is slightly increased compared with α-Fe_2O_3/Ag. Figure 3b,c is the corresponding TEM images of α-Fe_2O_3/Ag/SiO_2 (ST = 10 nm), which clearly show that a thin SiO_2 layer is over the α-Fe_2O_3/Ag NPs and the average thickness of the layer is about 10 nm. Figure 3d−f shows the SEM and TEM images of α-Fe_2O_3/Ag/SiO_2 NPs prepared by using 0.6 mL of TEOS. The shape of α-Fe_2O_3/Ag/SiO_2 (ST = 60 nm) changes to be ellipse-like, and the Ag NPs become smaller grains with uniform distribution in the SiO_2 shell. The phenomenon can be interpreted as follows: the original Ag NPs have been etched by ammonia in the presence of oxygen and consequently result in a water-soluble complex $[Ag(NH_3)_2]^+$, which is reduced again and produced lots of smaller silver grains.[34,35] The large Ag NPs can be clearly observed, and the small Ag NPs still existed in the composite NPs. From the curves j and k in Figure 9a, the characteristic absorption peak of Ag can be observed, and the above results reveal that the Ag has been successfully introduced.

dx.doi.org/10.1021/am404700h | ACS Appl. Mater. Interfaces 2014, 6, 1113−1124

The morphology and structure of the α-Fe_2O_3/Ag/SiO_2/SnO_2 (S1) nanocomposites generated by SnO_2 shell deposited on the template of α-Fe_2O_3/Ag/SiO_2 (ST = 60 nm) NPs are characterized by SEM and TEM, as shown in Figure 4. Figure 4a shows a SEM image at low magnification, displaying a large number of α-Fe_2O_3/Ag/SiO_2/SnO_2 NPs with uniform size, ellipse structure, and good dispersion. The high-magnified SEM image (Figure 4b) clearly shows that S1 possesses double SnO_2 shell consisting of a dense inner wall and loose outer shell. Figure 4c,d shows the TEM images of the sample at low and high magnification, respectively. It can be seen that the core−shell particles are ca. 500 nm in length and ca. 300 nm in width, which have a thin SnO_2 inner shell of ca. 15 nm in thickness and a thick SnO_2 outer shell of ca. 45 nm in thickness. Only one α-Fe_2O_3 spindle exists in most of the encapsulated NPs but most of the α-Fe_2O_3 cores are not located in the center of the nanocomposites. The phenomenon can be interpreted as follows: the silica interlayer is dissolved and becomes porous in the coating process of the SnO_2 shell by the hydrothermal method, which leads to the α-Fe_2O_3 spindles being free to move in the NPs.[36] More importantly, it is clearly observed from Figure 4d that the sample of S1 is the multilayer core−shell structure which contains a α-Fe_2O_3 spindle core, a porous silica interlayer, and an outer layer of double SnO_2 shells.

Further studies on the structure and composition of S1 are analyzed by HRTEM and EDX, as shown in Figure 5. Figure 5a shows the magnified TEM image of a single α-Fe_2O_3/Ag/SiO_2/SnO_2 nanoparticle, and the core−shell−shell structure can be clearly observed. Figure 5b shows the EDX spectra collected from four different locations within the Figure 5a (marked by numbers from 1 to 4). In the EDX spectra, the signals of Sn, Si, and O are all clearly observed, indicating the existence of SiO_2 and SnO_2 in S1. However, the signals from Ag element are also observed in the EDX spectra of the four spots, which implied that the Ag NPs are located in all layers. As expected, the signal from Fe element can only be detected in the central position of the α-Fe_2O_3/Ag/SiO_2/SnO_2 nanoparticle. The results indicate that the spindle-like α-Fe_2O_3 particle was encapsulated inside the core−shell hybrid structure. The HRTEM image (Figure 5c) reveals that the deposited SnO_2 shell is well crystallized with the d_{110} and d_{101} of rutile SnO_2 and exhibits highly mesoporous structures. In fact, the formation of SnO_2 is due to the following reactions: $K_2SnO_3 + CO_2$ (urea hydrolysis) → $SnO_2 \downarrow + K_2CO_3$.[37]

The crystalline phase and structure of α-Fe_2O_3, α-Fe_2O_3/Ag, Fe_2O_3/Ag/SiO_2 (ST = 60 nm), and S1 are confirmed by XRD analysis, as shown in Figure 6. The XRD pattern of α-Fe_2O_3 agrees well with the hexagonal phase of hematite (JCPDS No. 33-0664). Besides the diffraction peaks of hematite, α-Fe_2O_3/Ag also contains the peaks of the *fcc* Ag, consistent with the literature values (JCPDS No. 04-0783). After coating with SiO_2 structures, the peaks of hematite still existed and the intensity of Ag peaks became weak. However, there is no diffraction peaks of SiO_2 due to the amorphous nature of SiO_2. As for the sample of S1, the new additional peaks at 26.61, 33.87, 37.98, 51.74, 64.71, and 65.94 can be attributed to (110), (101), (200), (211), (112), and (301) planes of the tetragonal rutile SnO_2 (JCPDS No. 41-1445). Simultaneously, the peaks of hematite in S1 become weak, which is because the diffraction peak intensity of SnO_2 is much stronger than that of α-Fe_2O_3. The diffraction peaks of Ag become much weaker after being coated by SiO_2 and SnO_2 shells because of the very small size and low mass fraction of the Ag NPs,[38] but the existence of Ag

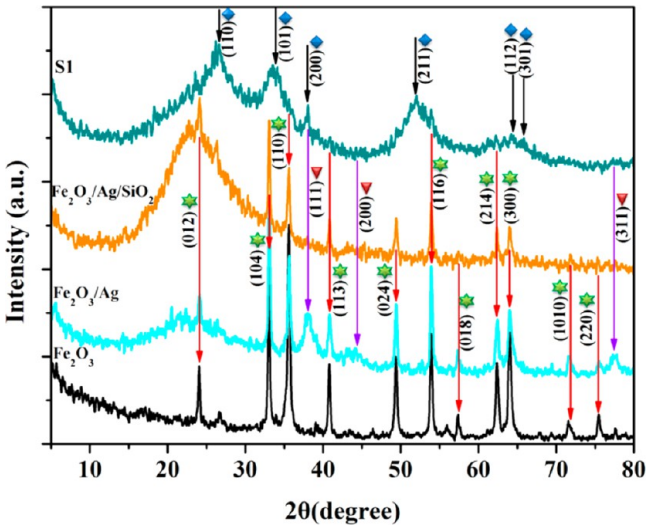

Figure 6. XRD patterns of the α-Fe_2O_3, α-Fe_2O_3/Ag, α-Fe_2O_3/Ag/SiO_2 (ST = 60 nm), and α-Fe_2O_3/Ag/SiO_2/SnO_2 (S1).

in S1 can be proven by the subsequent XPS results. The XRD analysis of S2 and S3 is also carried out in Figure S1a,b (see Supporting Information). The results demonstrate the existence of α-Fe_2O_3, SnO_2, and Ag in samples S2 and S3.

The surface properties of α-Fe_2O_3, α-Fe_2O_3/Ag, Fe_2O_3/Ag/SiO_2 (ST = 60 nm), and S1 are further studied by XPS analysis. Figure 7a shows the complete XPS spectra from 0 to 1400 eV of the samples. The survey spectra of α-Fe_2O_3, α-Fe_2O_3/Ag contain the peaks of Fe 2p while the Fe_2O_3/Ag/SiO_2 (ST = 60 nm) was not observed; this is probably because the inner α-Fe_2O_3 core was in center of the Fe_2O_3/Ag/SiO_2 NPs and thus too far away from the particle surface to be detected. After SnO_2 coating, the Fe2p signal is reobserved, due to the silica layer being less dense and resulting in a smaller concentration by the ammonia etching (from the urea decomposition).[39,40] The peaks of Ag 3d appearing in the curves of Fe_2O_3/Ag, Fe_2O_3/Ag/SiO_2 (ST = 60 nm), and S1 demonstrate that the silver exists in the hybrid structure. S1 synthesized by the SnO_2 deposited on the Fe_2O_3/Ag/SiO_2 NPs was proven by the appearance of the Sn 3d peaks. The survey spectra of samples S2 and S3 were shown in Figure S2a,b (see Supporting Information), respectively. The peaks of Fe 2p, Ag 3d, and Sn 3d appear in the curves of S2 and S3, which means the samples of S2 and S3 both contained α-Fe_2O_3, Ag, and SnO_2. Figure 7b displays the XPS spectrum of the region corresponding to the binding energy range of 500−475 eV and two peaks with binding energies at 486.4 and 494.9 eV; they are attributed to Sn $3d_{5/2}$ and Sn $3d_{3/2}$ of SnO_2, respectively, which illustrates the existence of tin oxide after SnO_2 coating. Figure 7c presents the XPS spectra of the Ag 3d peak from the samples of α-Fe_2O_3/Ag and α-Fe_2O_3/Ag/SiO_2 (ST = 60 nm). Two peaks in the curves of the two samples at 367.9 and 373.9 eV can be indexed to Ag $3d_{5/2}$ and Ag $3d_{3/2}$ of Ag^0, respectively, meaning that the α-Fe_2O_3/Ag and α-Fe_2O_3/Ag/SiO_2 NPs contained Ag NPs. The SEM, TEM, EDX, XRD, and XPS results confirms the formation of multilayer α-Fe_2O_3/Ag/SnO_2 ternary hybrid architectures.

The samples S2 and S3 are also characterized by electron microscopy. As shown in Figure 8a−c, the morphology and structure of the as-prepared α-Fe_2O_3/Ag/SiO_2/SnO_2 (S2, ST = 10 nm) are characterized by SEM and TEM. Most of the NPs

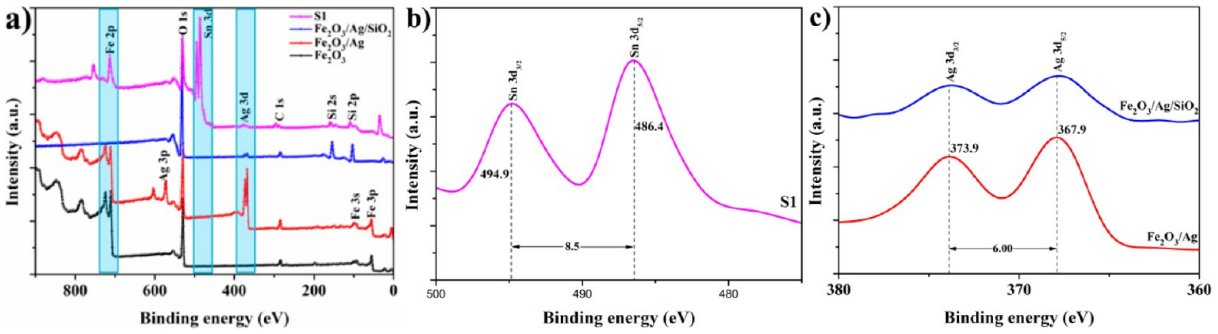

Figure 7. (a) The complete XPS spectra of the samples (Fe_2O_3, Fe_2O_3/Ag, Fe_2O_3/Ag/SiO_2 (ST = 60 nm), and S1); (b) main and satellite peak of Sn $3d_{3/2}$ and Sn $3d_{1/2}$ for the sample S1; (c) main and satellite peak of Ag $3d_{5/2}$ and Ag $3d_{3/2}$ peak for the α-Fe_2O_3/Ag NPs and α-Fe_2O_3/Ag/SiO_2 (ST = 60 nm).

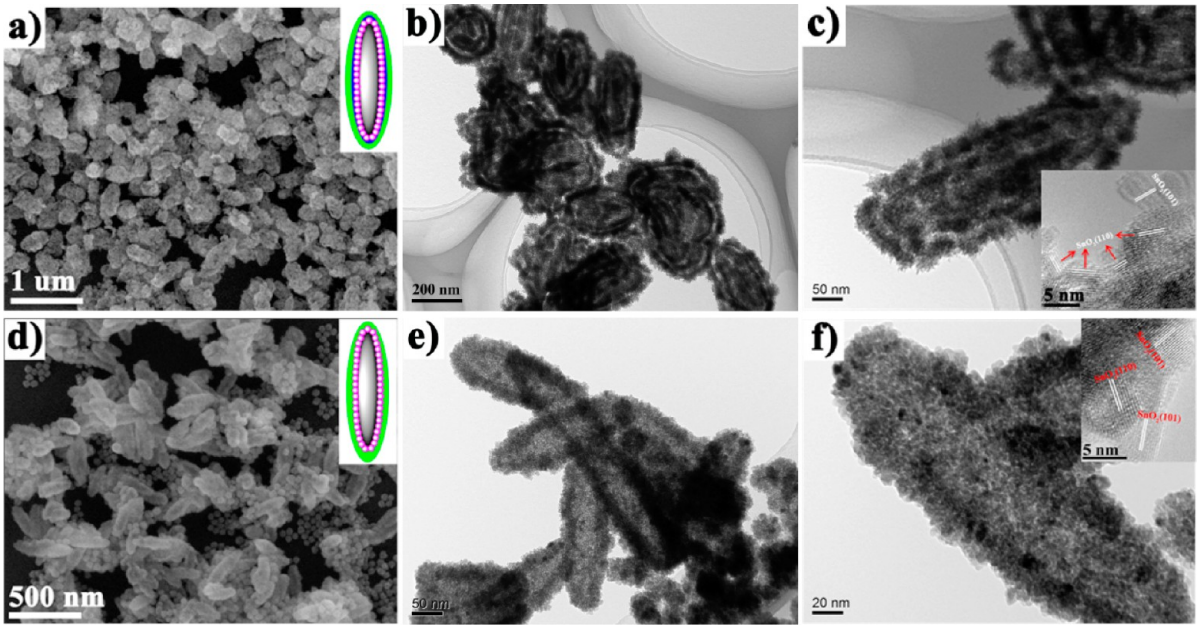

Figure 8. SEM (a) and TEM (b, c) images of the α-Fe_2O_3/Ag/SiO_2/SnO_2 (S2) nanocomposites; SEM (d) and TEM (e, f) images of the α-Fe_2O_3/Ag/SnO_2 (S3) nanocomposites (the insets are a structural model and HRTEM image, respectively).

possessing double-layered SnO_2 and ellipse-like shape with a size of ca. 500 nm in length and ca. 200 nm in width can be clearly observed. The inset HRTEM image in Figure 8c demonstrates that the outer shell is a SnO_2 layer consisting of rutile SnO_2 NPs with crystalline lattice of d_{110} and d_{101}. Figure 8d–f shows the SEM and TEM images of α-Fe_2O_3/Ag/SnO_2 (S3, ST = 0 nm). The morphology of S3 still has a spindle-like shape. It can be observed that the NPs have uniform size of ca. 300 nm in length and ca. 100 nm in width. The average thickness of the porous SnO_2 layer is about 20 nm. In addition, the synthesized α-Fe_2O_3/SnO_2 nanocomposites as a sample without Ag NPs are characterized by SEM and HRTEM (in the Supporting Information). The corresponding SEM image (Figure S3a), HRTEM images (Figure S3b,c) and the EDX analysis (Figure S3d) illustrate that the α-Fe_2O_3/SnO_2 NPs were successfully synthesized with well-dispersed and uniform size with a length of ca. 280 nm and a width of ca. 90 nm.

Figure 9a shows the UV–visible spectra of all the samples. The α-Fe_2O_3 nanospindles (curve b) have a visible absorption band from 380 to 600 nm due to the narrow band gap of α-Fe_2O_3 (~2.2 eV). After Ag coating, the α-Fe_2O_3/Ag sample (curve h) possesses a strong absorption peak around 400 nm, indexing to the typical surface plasmon resonance (SPR) absorption of silver NPs. Moreover, the absorption band of the sample becomes wide. The red-shift of the UV–visible absorption is due to the introduction of Ag NPs. The SPR absorption peak of silver in the absorption spectra of α-Fe_2O_3/Ag/SiO_2 (ST = 60 nm) NPs (curve k) and α-Fe_2O_3/Ag/SiO_2 (ST = 10 nm) NPs (curve j) can also be detected. Compared with the pure α-Fe_2O_3 NPs, the α-Fe_2O_3/Ag/SiO_2/SnO_2 nanocomposites (S1, S2, and S3) have obvious enhancement of UV absorption due to the coating of SnO_2 shell.

The photocatalytic activities of the α-Fe_2O_3/Ag/SiO_2/SnO_2 nanocomposites with different thicknesses of silica interlayer are measured by the degradation of RhB aqueous solution under UV and visible mixed light, and the pure α-Fe_2O_3 seeds, commercial SnO_2 NPs, and α-Fe_2O_3/SnO_2 nanocomposites are also measured for comparison. The absorption spectra during the photodegradation of RhB under UV and visible mixed light are shown in Figure S4 (see Supporting Information). In general, the photodegradation of RhB catalyzed by the semiconductor nanomaterials follows a pseudo-first-order rate law,[41−43] $-\ln(C/C_0) = Kt$, where K is the apparent rate constant of the degradation, C_0 and C are the concentrations of

dx.doi.org/10.1021/am404700h | ACS Appl. Mater. Interfaces 2014, 6, 1113–1124

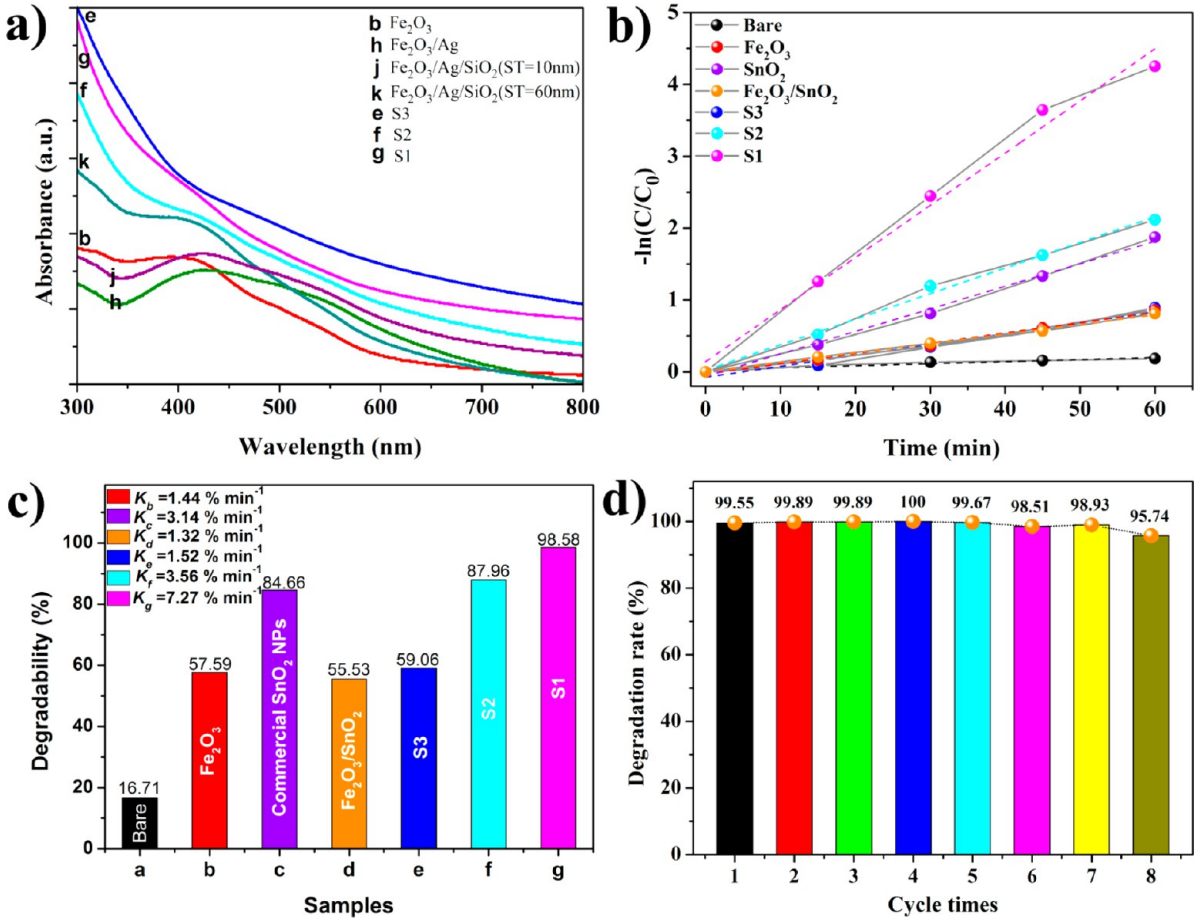

Figure 9. (a) UV–visible absorption spectra of all the samples obtained in our work including (b) α-Fe_2O_3, (h) α-Fe_2O_3/Ag (ST = 0 nm), (j) α-Fe_2O_3/Ag/SiO_2 (ST = 10 nm), (k) α-Fe_2O_3/Ag/SiO_2 (ST = 60 nm), (e) S3, (f) S2, and (g) S1; (b) the apparent reaction rate constant versus irradiation time of UV and visible mixed light in the presence of different catalysts; (c) the degradability distributions of all the catalysts in (b) under UV and visible mixed light irradiation for 60 min; (d) recycled photodegradations of RhB under the irradiation of UV and visible mixed light for 90 min over the sample S1.

RhB at initial and at a certain irradiation time *t*, respectively. As shown in Figure 9b, the results illustrate that both S1 and S2 have rapid degradation rates which are much higher than the pure α-Fe_2O_3 seeds, commercial SnO_2 NPs, and α-Fe_2O_3/SnO_2 nanocomposites. S3 also has enhanced photocatalytic activity compared with the pure α-Fe_2O_3 and α-Fe_2O_3/SnO_2 nanocomposites. The degradation rate in 60 min and the corresponding *K* values of the photocatalysts are summarized in Figure 9c. The results confirm that S1 exhibits the best photocatalytic activity (degradation rate can reach 98.58%) among the measured samples. In addition, the degradation rates of S2 and S3 can reach 87.96% and 59.06%, respectively. Obviously, the thickness of silica has a great influence on the photocatalytic activity in the multilayer core–shell α-Fe_2O_3/Ag/SiO_2/SnO_2 nanocomposites that results from the photocatalytic activity of ST = 60 nm being better than the others. More importantly, the α-Fe_2O_3/Ag/SnO_2 ternary hybrid architectures display clearly enhanced photocatalytic abilities for RhB, and the degradation rates of samples S2 and S3 are higher than the pure α-Fe_2O_3 seeds, commercial SnO_2 nanopowders (70 nm), and α-Fe_2O_3/SnO_2 nanocomposites. Figure 9d displays the durability of photocatalytic activity of S1 for the degradation of RhB under illumination. It clearly shows that the catalytic performance of the catalyst for photocatalytic degradation of RhB remains approximately constant even after eight cycles. Especially at the eighth cycle, the degradation rate of RhB solution can still be maintained at 95.74%. The results of photocatalytic experiments illustrate that the S1 nanocomposites not only possess enhanced photocatalytic activity under UV and visible mixed light but also exhibit good recyclability due to the stable durability of photocatalytic activity.

To further study the influence on the photocatalytic activity of the thickness of the silica interlayer, the catalytic performance of the composites are also measured under the irradiation of UV light and visible light, respectively. As shown in Figure 10, the degradation rates of different α-Fe_2O_3/Ag/SnO_2 ternary hybrid architectures under the irradiation of UV light or visible light have been investigated, and the reaction time was prolonged to 180 min to better study the photocatalytic activity of the samples. Under the illumination of UV light (Figure 10a,b), the degradation rate of S1 is also highest among the three samples and can reach 51.26%, which is much more than that of S2 (13.94%) and S3 (27.19%). However, as shown in Figure 10c,d, the sample of S3 exhibits enhanced photocatalytic activity under illumination of visible light, and its degradation rate can reach 96.99% while the degradation rates of S1 and S2 are only 19.10% and 14.34%, respectively. As a comparison, the degradation rates of α-Fe_2O_3/SnO_2 nanocomposites under the irradiation of UV light or visible light

dx.doi.org/10.1021/am404700h | *ACS Appl. Mater. Interfaces* 2014, 6, 1113–1124

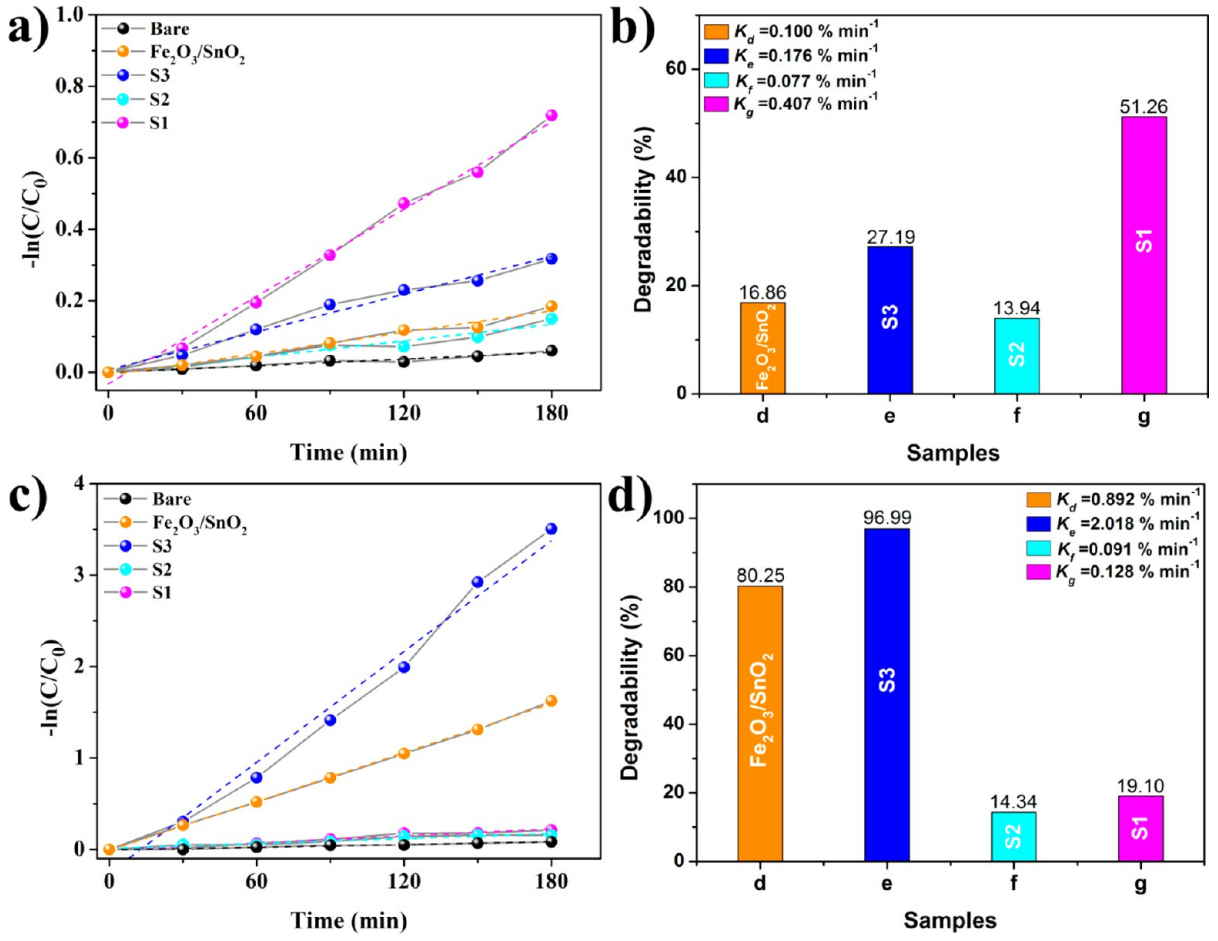

Figure 10. The performances and degradation rate of the samples of α-Fe_2O_3/SnO_2, S1, S2, and S3 for the degradation of RhB solution under the irradiation of UV light (λ < 420 nm) (a, b) and visible light (λ > 420 nm) (c, d).

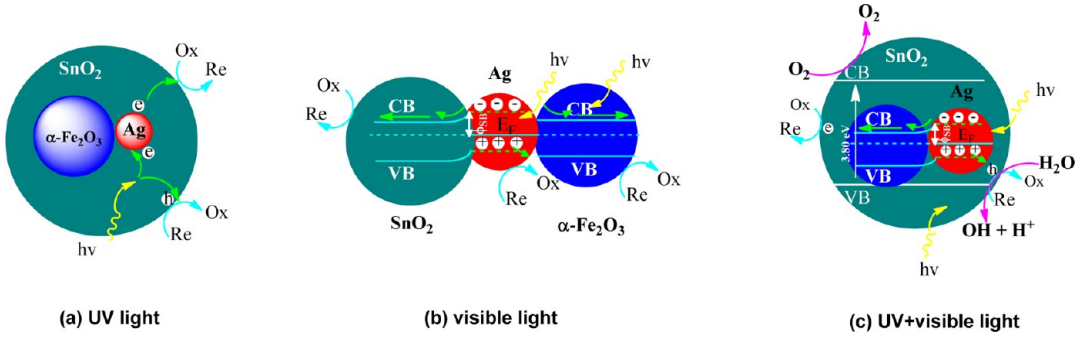

Figure 11. Schematic diagram for band configuration and electron–hole separation at the interface of α-Fe_2O_3/Ag/SnO_2 ternary hybrid architectures under different light irradiation with three approaches: SnO_2 being activated (a, UV light, λ < 420 nm, mainly SnO_2 excited), Ag and α-Fe_2O_3 being activated (b, visible light, λ > 420 nm), and SnO_2, Ag, and α-Fe_2O_3 being activated simultaneously (c, UV and visible mixed light).

have been investigated and shown in Figure 10a–d. Compared to the α-Fe_2O_3/SnO_2 sample without Ag NPs, the α-Fe_2O_3/Ag/SnO_2 nanocomposites (S3) all have enhancement in photodegradation rate whether under UV light irradiation or under visible light irradiation. That means the introduced Ag NPs have influence on the photocatalytic activity due to the LSPR effect and scattering effect. Compared with the samples S1 and S2, the α-Fe_2O_3/SnO_2 NPs exhibit an enhanced photocatalytic activity under visible light irradiation due to the size of α-Fe_2O_3/SnO_2 NPs being smaller than those in samples S1 and S2, resulting in an increasing amount of α-Fe_2O_3/SnO_2 NPs, which means that more α-Fe_2O_3 nanospindles can be excited by visible light. Furthermore, the formed Fe_2O_3–SnO_2 heterostructures of α-Fe_2O_3/SnO_2 NPs can effectively mitigate the recombination between photogenerated electron–hole pairs by the electrons being transferred from α-Fe_2O_3 to SnO_2 under visible light irradiation.

Metal oxide semiconductors (such as TiO_2, SnO_2, and ZnO) have been commonly regarded as benchmark photocatalysts, and their role in the relevant area has been substantially studied for decades. However, the relatively wide band gap of SnO_2 limits its absorption to only UV light, while the faster recombination rate of electron–hole pairs reduces its catalytic efficiency. The loading of noble metal on the surface of metal

dx.doi.org/10.1021/am404700h | ACS Appl. Mater. Interfaces 2014, 6, 1113–1124

oxide semiconductor can enhance the photocatalytic property in two ways. First, the incorporated noble metal NPs can act as electron traps, leading to facile electron−hole separation, which is utilized mainly under the exposure of UV light. Second, the SPR effect induced by visible light irradiation can be used to enhance the activity of photocatalysts.[44] In the current α-Fe_2O_3/Ag/SnO_2 ternary hybrid architectures, the noble metal Ag NPs have been loaded on the surface of α-Fe_2O_3 (narrow band gap semiconductor), and the interlayer SiO_2 has been introduced and employed to tailor the photocatalytic abilities. Moreover, loading a SiO_2 interlayer between Ag and SnO_2 not only can minimize the damping and forbid the electron transfer effectively when a metal is placed in direct contact with a semiconductor but also can protect the Ag NPs. Herein, the SiO_2 interlayer represents a buffer that keeps the SnO_2 and Ag at a finite distance from each other without physically touching, providing an environment where the negative effect of the Foster energy transfer is diminished. However, the local electric field amplitude decays with the distance from the surface of Ag NPs. Therefore, the thickness of the SiO_2 layer can be used to regulate PRET and the distance of different semiconductors (α-Fe_2O_3 and SnO_2) and finally tailor the photocatalytic abilities. The proposed mechanism of photocatalytic decomposition of RhB by α-Fe_2O_3/Ag/SnO_2 ternary hybrid architectures was shown in Figure 11.

Under UV light, Ag can lead to the interfacial charge transfer and the decrease in the recombination rate by trapping the excitons. This is attributed to the lower Fermi energy of noble metal Ag, which can serve as a reservoir for photoinduced charge carriers and extend the lifetime of the electron−hole pairs.[45] When Ag NPs come into contact with α-Fe_2O_3, they retain charge and lead the net Fermi level to shift to a more negative potential. The photogenerated electrons in α-Fe_2O_3 are transferred to Ag, and this continues until they attain equilibrium. At this moment, the SiO_2 interlayer is better for tailoring the PIRET since the energy transfer from Ag NPs to SnO_2 does not require direct contact.[28] When the Ag NPs come in direct contact with SnO_2, the energetic electrons are injected from Ag NPs to SnO_2, increasing the recombination rate of the electron−hole pairs (although the Schottky contact promotes the increase of the separation rate of the electron−hole pairs).[46] Therefore, the electron transfer from Ag to SnO_2 makes a negative contribution to the photocatalytic activity, which would result in sample S3 processing a lower photocatalytic performance. Under visible light, SnO_2 has no absorption response to the visible light due to its wide band gap; thus, Ag NPs and α-Fe_2O_3 contributed to the light absorption of α-Fe_2O_3/Ag/SnO_2 ternary hybrid architectures (Figure 11b). As the conduction band of SnO_2 is around 0 V vs NHE and the Fermi level for Ag is about 0.4 V vs NHE, energetic electrons generated by the SPR under visible light irradiation can be transferred from the metal to the semiconductor. In fact, the work function (ϕ) of Ag is 4.26, and the n-type semiconductor SnO_2 is 4.4; the electrons are accumulated in the space charge region due to the electron transfer from the metal to the semiconductor, and this region is called the accumulation layer. In general, when the Fermi level of the metal is below that of the semiconductor, charge will flow to the metal causing the semiconductor Fermi level to decrease, and vice versa.[26,47] On one hand, the near field enhancement by SPR of Ag can increase the charge carrier generation, resulting in enhancement of the photocurrent. When the efficiency of scattering is controlled by the size of NPs, the efficiency of near field enhancement is influenced by the size of the NPs and the interparticle space between them. Larger α-Fe_2O_3 particles can effectively scatter the incoming light compared to smaller particles and can increase the decay length of the localized field. On the other hand, the α-Fe_2O_3 and SnO_2 will form a contact interface without the silica interlayer, and the above structure between two semiconductors with a narrow and wide band gap is beneficial to enhance the photocatalytic abilities.[32,48] Therefore, the photocatalytic performance of sample S3 is best. The UV and visible light resource was used to simulate the sunlight environment; the corresponding charge injection mechanism may be very complicated. The energetic electrons are generated in the conduction band of SnO_2 under UV light, and they can transfer from SnO_2 to Ag due to their energy alignment. At the same time, the metallic plasmonic Ag NPs essentially act as a dye sensitizer, absorbing resonant photons and transferring the energetic electron, formed in the process of the SPR excitation, to the nearby α-Fe_2O_3 and SnO_2 semiconductor, and the SiO_2 interlayer can be tailored for the two extremes of the Förster resonant energy transfer (FRET) and the LSPR enhancement, which is in general attained for the distance of a few nanometers between the metal and semiconductors. (Though the silica thickness of S1 is 60 nm, the Ag NPs have been redispersed in silica interlayer, as shown in Figure 3f.) Therefore, we conclude that more electrons are photogenerated in the S1 than the other two samples because of synergistic effects between SnO_2-based conventional semiconductor photocatalysis and Ag/α-Fe_2O_3 plasmonic visible light-driven photocatalysis.

The photocatalytic activities of the samples of S1, S2, and S3 under the irradiation of UV light, visible light, and UV and visible mixed light are summarized in Figure 12. As shown in Figure 12, the degradation rate of samples S1, S2, and S3 under the irradiation of UV and visible mixed light irradiation can reach 98.58%, 87.96%, and 59.06% in 60 min, respectively. The photocatalytic activity of S1 is also higher than the samples of S2 and S3 under the irradiation of UV light. However, the sample of S3 exhibits excellent visible light photocatalytic ability superior to other samples. Furthermore, the photocatalytic

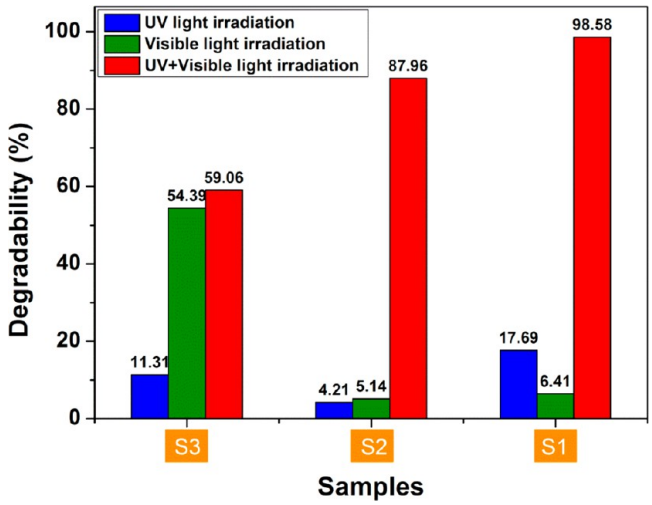

Figure 12. The comparison for the degradation rate of samples S1, S2, and S3 in 60 min under the irradiation of UV light (λ < 420 nm), visible light (λ > 420 nm), and UV and visible mixed light, respectively.

activity of the sample with a thinner silica layer is exhibited excellently under irradiation of visible light, superior to the irradiation of UV light. Hence, photocatalytic activities of the current hybrid structures can be adjusted to the different illumination resources by tailoring the thickness of the silica interlayer.

CONCLUSIONS

In summary, we presented a successful synthesis of multicomponent and multifunctional α-Fe_2O_3/Ag/SiO_2/SnO_2 NPs with well-defined core−shell−shell structures, which consisted of narrow and wide band gap semiconductors, doped catalytic silver NPs, and a controlled silica interlayer. The as-obtained multilayer structure nanocomposites have been applied to photocatalytic activity research. To study the catalytic mechanism of the nanocomposites and tailor the coupling effect of the interface between noble metal and semiconductor, the samples with different thicknesses of silica interlayer were synthesized. The results of catalytic tests illustrated that α-Fe_2O_3/Ag/SiO_2/SnO_2 nanocomposites with thicker silica interlayer exhibit higher photocatalytic activity, good stability, and recyclability under the irradiation of UV and visible mixed light. Because of the simplicity and feasibility of the process, it is believed that this strategy will be suitable for scalable fabrication. On the other hand, because of their unique structure, the as-prepared α-Fe_2O_3/Ag/SnO_2 ternary hybrid architectures with uniform shape and composition are expected to provide new insights in various applications such as gas sensors, lithium batteries, and photocatalysis.

ASSOCIATED CONTENT

Supporting Information

The parameters of the used mercury lamp in the photocatalytic tests, XRD patterns and XPS spectra of samples S2 and S3, SEM image, HRTEM image, EDX spectra of α-Fe_2O_3/SnO_2 NPs, UV−vis spectra of the photodecomposition of RhB dye in solution over the different samples under UV and visible mixed light irradiation for various time periods, and the apparent reaction rate constant versus irradiation time of visible light in the presence of the sample of pure α-Fe_2O_3 NPs and sample S3. This information is available free of charge via the Internet at http://pubs.acs.org.

AUTHOR INFORMATION

Corresponding Authors

*E-mail: weiwu@whu.edu.cn.
*E-mail: czjiang@whu.edu.cn.

Notes

The authors declare no competing financial interest.

ACKNOWLEDGMENTS

The authors want to thank Dr. Lixia Fan (WUST) for SEM analyses. The authors also thank the NSFC (51201115, 51171132, 11375134), Young Chenguang Project of Wuhan City (2013070104010011), China Postdoctoral Science Foundation (2012M511661), and the Fundamental Research Funds for the Central Universities.

REFERENCES

(1) Joo, J. B.; Zhang, Q.; Dahl, M.; Lee, I.; Goebl, J.; Zaera, F.; Yin, Y. *Energy Environ. Sci.* **2012**, *5*, 6321−6327.
(2) Wu, S. S.; Cao, H. Q.; Yin, S. F.; Liu, X. W.; Zhang, X. R. *J. Phys. Chem. C* **2009**, *113*, 17893−17898.
(3) Karunakaran, C.; Senthilvelan, S. *Electrochem. Commun.* **2006**, *8*, 95−101.
(4) Xi, G. C.; Yan, Y.; Ma, Q.; Li, J. F.; Yang, H. F.; Lu, X. J.; Wang, C. *Chem.—Eur. J.* **2012**, *18*, 13949−13953.
(5) Yang, J. L.; An, S. J.; Park, W. I.; Yi, G. C.; Choi, W. *Adv. Mater.* **2004**, *16*, 1661−1665.
(6) Li, L.; Xu, L.; Shi, W.; Guan, J. *Int. J. Hydrogen Energy* **2012**, *38*, 816−822.
(7) Tong, G.; Guan, J.; Zhang, Q. *Mater. Chem. Phys.* **2011**, *127*, 371−378.
(8) Huang, X.; Guan, J.; Xiao, Z.; Tong, G.; Mou, F.; Fan, X. a. *J. Colloid Interface Sci.* **2011**, *357*, 36−45.
(9) Davis, M.; Hikal, W. M.; Gümeci, C.; Hope-Weeks, L. J. *Catal. Sci. Technol.* **2012**, *2*, 922−924.
(10) Zheng, L.; Zheng, Y.; Chen, C.; Zhan, Y.; Lin, X.; Zheng, Q.; Wei, K.; Zhu, J. *Inorg. Chem.* **2009**, *48*, 1819−1825.
(11) Zhang, Z.; Shao, C.; Li, X.; Zhang, L.; Xue, H.; Wang, C.; Liu, Y. *J. Phys. Chem. C* **2010**, *114*, 7920−7925.
(12) Li, X.; John, V. T.; Zhan, J.; He, G.; He, J.; Spinu, L. *Langmuir* **2011**, *27*, 6252−6259.
(13) Mou, F.; Xu, L.; Ma, H.; Guan, J.; Chen, D.-r.; Wang, S. *Nanoscale* **2012**, *4*, 4650−4657.
(14) Sun, L. L.; Wu, W.; Zhang, S. F.; Zhou, J.; Cai, G. X.; Ren, F.; Xiao, X. H.; Dai, Z. G.; Jiang, C. Z. *AIP Adv.* **2012**, *2*, 032179.
(15) Niu, M. T.; Huang, F.; Cui, L. F.; Huang, P.; Yu, Y. L.; Wang, Y. S. *ACS Nano* **2010**, *4*, 681−688.
(16) Ponja, S.; Sathasivam, S.; Chadwick, N.; Kafizas, A.; Bawaked, S. M.; Obaid, A. Y.; Al-Thabaiti, S.; Basahel, S. N.; Parkin, I. P.; Carmalt, C. J. *J. Mater. Chem. A* **2013**, *1*, 6271−6278.
(17) Yang, G. D.; Yan, Z. F.; Xiao, T. C. *Appl. Surf. Sci.* **2012**, *258*, 8704−8712.
(18) Xu, L.; Guan, J.; Shi, W. *ChemCatChem* **2012**, *4*, 1353−1359.
(19) Liu, X.; Zhang, J.; Guo, X.; Wang, S.; Wu, S. *RSC Adv.* **2012**, *2*, 1650−1655.
(20) Zhu, L.-P.; Bing, N.-C.; Yang, D.-D.; Yang, Y.; Liao, G.-H.; Wang, L.-J. *CrystEngComm* **2011**, *13*, 4486−4490.
(21) Niu, M.; Huang, F.; Cui, L.; Huang, P.; Yu, Y.; Wang, Y. *ACS Nano* **2010**, *4*, 681−688.
(22) Wu, W.; Zhang, S. F.; Ren, F.; Xiao, X. H.; Zhou, J.; Jiang, C. Z. *Nanoscale* **2011**, *3*, 4676−4684.
(23) Zhang, S. F.; Ren, F.; Wu, W.; Zhou, J.; Xiao, X. H.; Sun, L. L.; Liu, Y.; Jiang, C. Z. *Phys. Chem. Chem. Phys.* **2013**, *15*, 8228−8236.
(24) Moores, A.; Goettmann, F. *New J. Chem.* **2006**, *30*, 1121−1132.
(25) Tong, H.; Ouyang, S.; Bi, Y.; Umezawa, N.; Oshikiri, M.; Ye, J. *Adv. Mater.* **2012**, *24*, 229−251.
(26) Zhang, Z.; Yates, J. T. *Chem. Rev.* **2012**, *112*, 5520−5551.
(27) Zhang, N.; Liu, S.; Xu, Y.-J. *Nanoscale* **2012**, *4*, 2227−2238.
(28) Cushing, S. K.; Li, J.; Meng, F.; Senty, T. R.; Suri, S.; Zhi, M.; Li, M.; Bristow, A. D.; Wu, N. *J. Am. Chem. Soc.* **2012**, *134*, 15033−15041.
(29) Tian, Y.; Tatsuma, T. *J. Am. Chem. Soc.* **2005**, *127*, 7632−7637.
(30) Khan, M. M.; Ansari, S. A.; Amal, M. I.; Lee, J.; Cho, M. H. *Nanoscale* **2013**, *5*, 4427−4435.
(31) Moonsiri, M.; Rangsunvigit, P.; Chavadej, S.; Gulari, E. *Chem. Eng. J.* **2004**, *97*, 241−248.
(32) Wu, W.; Zhang, S. F.; Xiao, X. H.; Zhou, J.; Ren, F.; Sun, L. L.; Jiang, C. Z. *ACS Appl. Mater. Interfaces* **2012**, *4*, 3602−3609.
(33) Zhang, S. F.; Ren, F.; Wu, W.; Zhou, J.; Sun, L. L.; Xiao, X. H.; Jiang, C. Z. *J. Nanopart. Res.* **2012**, *14*, 1105.
(34) Lu, X.; Au, L.; McLellan, J.; Li, Z.-Y.; Marquez, M.; Xia, Y. *Nano Lett.* **2007**, *7*, 1764−1769.
(35) Cobley, C. M.; Rycenga, M.; Zhou, F.; Li, Z.-Y.; Xia, Y. *J. Phys. Chem. C* **2009**, *113*, 16975−16982.
(36) Kamata, K.; Lu, Y.; Xia, Y. *J. Am. Chem. Soc.* **2003**, *125*, 2384−2385.
(37) Wu, W.; Zhang, S. F.; Zhou, J.; Xiao, X. H.; Ren, F.; Jiang, C. Z. *Chem.—Eur. J.* **2011**, *17*, 9708−9719.

(38) Cui, B.; Peng, H.; Xia, H.; Guo, X.; Guo, H. *Sep. Purif. Technol.* **2013**, *103*, 251−257.
(39) Tunc, I.; Suzer, S.; Correa-Duarte, M. A.; Liz-Marzan, L. M. *J. Phys. Chem. B* **2005**, *109*, 7597−7600.
(40) Shard, A. G. *J. Phys. Chem. C* **2012**, *116*, 16806−16813.
(41) Wang, G.; Lu, W.; Li, J. H.; Choi, J.; Jeong, Y. S.; Choi, S. Y.; Park, J. B.; Ryu, M. K.; Lee, K. *Small* **2006**, *2*, 1436−1439.
(42) Liu, Z. Y.; Sun, D. D. L.; Guo, P.; Leckie, J. O. *Nano Lett.* **2007**, *7*, 1081−1085.
(43) Wu, W.; Liao, L.; Zhang, S. F.; Zhou, J.; Xiao, X. H.; Ren, F.; Sun, L. L.; Dai, Z. G.; Jiang, C. Z. *Nanoscale* **2013**, *5*, 5628−5636.
(44) Kochuveedu, S. T.; Jang, Y. H.; Kim, D. H. *Chem. Soc. Rev.* **2013**, *42*, 8467−8493.
(45) Subramanian, V.; Wolf, E. E.; Kamat, P. V. *J. Am. Chem. Soc.* **2004**, *126*, 4943−4950.
(46) Zhou, J.; Ren, F.; Zhang, S.; Wu, W.; Xiao, X.; Liu, Y.; Jiang, C. *J. Mater. Chem. A* **2013**, *1*, 13128−13138.
(47) Sarina, S.; Waclawik, E. R.; Zhu, H. *Green Chem.* **2013**, *15*, 1814−1833.
(48) Vinu, R.; Madras, G. *J. Indian Inst. Sci.* **2010**, *90*, 189−230.